





# Optical spin initialization of spin- $\frac{3}{2}$ silicon vacancy centers in 6H-SiC at room temperature

Harpreet Singh <sup>1,\*</sup>, Andrei N. Anisimov <sup>2</sup>, Ilia D. Breev <sup>2</sup>, Pavel G. Baranov,<sup>2</sup> and Dieter Suter <sup>1</sup>

<sup>1</sup>*Fakultät Physik, Technische Universität Dortmund, D-44221 Dortmund, Germany*

<sup>2</sup>*Ioffe Institute, St. Petersburg 194021, Russia*



(Received 14 July 2020; accepted 26 February 2021; published 11 March 2021)

Silicon vacancies in silicon carbide have been proposed as an alternative to nitrogen vacancy centers in diamonds for spintronics and quantum technologies. An important precondition for these applications is the initialization of the qubits into a specific quantum state. In this work, we study the optical alignment of the spin  $3/2$  negatively charged silicon vacancy in 6H-SiC. Using time-resolved optically detected magnetic resonance, we coherently control the silicon vacancy spin ensemble and measure Rabi frequencies, spin-spin and spin-lattice relaxation times of all three transitions. Then to study the optical initialization process of the silicon vacancy spin ensemble, the vacancy spin ensemble is prepared in different ground states and optically excited. We describe a simple rate equation model that can explain the observed behavior and determine the relevant rate constants.

DOI: [10.1103/PhysRevB.103.104103](https://doi.org/10.1103/PhysRevB.103.104103)

## I. INTRODUCTION

Silicon carbide (SiC) exists in many polytypes and hosts many interesting vacancy centers, which have been shown to be useful for applications in quantum technologies such as sensing [1–7]. These vacancy centers can be grouped into two classes, depending on their spin in the ground state:  $S = 1$  or  $3/2$  [8,9]. Neutral divacancies, consisting of neighboring C and Si vacancies, have spin 1. Four different types of divacancies in 4H-SiC have been studied using optical and microwave techniques [7] similar to those used with nitrogen-vacancy (NV) qubits in diamond [10–12]. They can be efficiently polarized by optical irradiation, and their polarization can be transferred to  $^{29}\text{Si}$  nuclear spins, which are strongly coupled to divacancies in 4H- and 6H-SiC [13]. Coherent control of divacancy spins in 4H-SiC can be achieved even at high temperature up to 600 K [14]. The spins of neutral divacancies in SiC can sensitively detect both strain and electric fields [15], with higher sensitivity than NV centers in diamond [1,15].

Another type of vacancy consists of missing silicon atoms, i.e., silicon vacancies. If they capture an additional electron, they become negatively charged silicon vacancies ( $V_{\text{Si}}^-$ ) and have spin  $3/2$  [4,8,9,16,17]. Several individually addressable silicon vacancies have been identified in different SiC polytypes. For example, the 6H-SiC hosts one hexagonal site  $h$  and two cubic sites ( $k_1$  and  $k_2$ ).  $V_{\text{Si}}^-$  at  $k_1$  and  $k_2$  are called  $V_1$  and  $V_3$ , respectively, whereas  $V_{\text{Si}}^-$  at the hexagonal sites  $h$  are called  $V_2$  [17,18]. Recently, it has been shown that  $V_{\text{Si}}^-$  at hexagonal lattice sites  $h$  corresponds to  $V_1$ , and at cubic lattice sites  $k_1$  and  $k_2$  they are  $V_3$  and  $V_2$ , respectively [19]. The zero phonon lines (ZPLs) of these negatively charged vacancies appear at 865 nm ( $V_1$ ), 887 nm ( $V_2$ ), and 908 nm ( $V_3$ ) [17,18,20]. Optically induced alignment of the ground-state spin sublevels of the  $V_{\text{Si}}^-$  in 4H- and 6H-SiC has been demonstrated at room

temperature [16]. Coherent control of a single silicon-vacancy spin and long spin coherence times have been reported [2].  $V_{\text{Si}}^-$  are relatively immune to electron-phonon interactions, and they do not exhibit fast spin dephasing (spin coherence time  $T_2 = 0.85$  ms) [21]. Using a moderate magnetic field in combination with dynamic decoupling, the spin coherence of the  $V_{\text{Si}}^-$  spin ensemble in 4H-SiC with natural isotopic abundance can be preserved over an unexpectedly long time of  $>20$  ms [22]. Quantum microwave emitters based on  $V_{\text{Si}}^-$  in SiC at room temperature [23] can be enhanced via fabrication of Schottky barrier diodes, and they can be modulated by almost 50% by an external bias voltage [24]. Using all four levels,  $V_{\text{Si}}^-$  can be used for absolute dc magnetometry [25].

In our previous work, we studied the temperature-dependent photoluminescence, optically detected magnetic resonance (ODMR), and the relaxation times of the longitudinal and transverse components of the  $V_{\text{Si}}^-$  spin ensemble in 6H-SiC, during free precession as well as under the influence of different refocusing schemes [20].

In this work, we focus on the optical spin initialization of the  $V_1/V_3$  in 6H-SiC, the spin relaxation, and the dynamics of the intersystem-crossing. Section II gives details of the optical pumping process. Section III describes the experimental setup for continuous-wave (cw) double-resonance and pulsed ODMR measurements. Section IV describes the measurements of the spin-lattice relaxation rates. Section V describes the dynamics of the optical spin alignment. Section VI contains a brief discussion and concluding remarks.

## II. SYSTEM

The experiments were performed on a sample that was isotopically enriched in  $^{28}\text{Si}$  and  $^{13}\text{C}$  [20]. The presence of 4.7%  $^{13}\text{C}$  reduces the coherence time of the vacancy spin centers [26]. Details of the sample preparation are given in Appendix A. In our previous work [20], photoluminescence (PL) spectra recorded at 5.4 K showed zero phonon lines

\*harpreet.singh@tu-dortmund.de

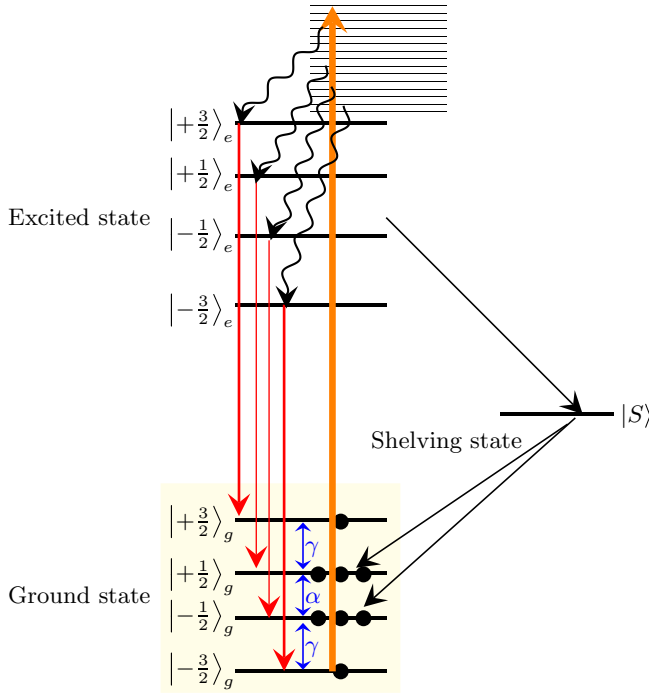


FIG. 1. Energy-level diagram of the  $6H$ -SiC  $V_1/V_3$  type  $V_{Si}^-$  showing the ground, excited, and shelving states. Radiative transitions are marked by red arrows. The nonresonant laser excitation is shown with an orange arrow. Spin-dependent nonradiative transitions generating the ground-state spin polarization are shown as black arrows. The states  $|\cdot\rangle_g$  represent ground states,  $|\cdot\rangle_e$  are the excited states, and  $|S\rangle$  are the shelving states.

(ZPLs) of the negatively charged vacancies at 865 nm ( $V_1$ ), 887 nm ( $V_2$ ), and 908 nm ( $V_3$ ).

The negatively charged  $V_1/V_3$ -type defect in  $6H$ -SiC has spin  $S = 3/2$  [8,9]. Figure 1 shows the relevant energy-level diagram in an external magnetic field. The states  $|\cdot\rangle_g$  are the spin states of electronic ground state [17,23], and  $|\cdot\rangle_e$  are the electronically excited states [27,28]. The shelving state  $|S\rangle$  is an  $S = 1/2$  state, which is important for the optical pumping process [27] during which it gets populated by intersystem crossing (ISC).

The spin Hamiltonian of the  $S = 3/2$  states is

$$\mathcal{H} = D(S_z^2 - \frac{5}{4}\hat{I}) + g\mu_B\vec{B} \cdot \vec{S}, \quad (1)$$

where the zero field splitting in the electronic ground state is  $2D = -28$  MHz for  $V_1/V_3$  [17,20],  $g = 2.0$  is the electron  $g$ -factor,  $\mu_B$  is the Bohr magneton,  $\hat{I}$  is the unit operator,  $\vec{B}$  is the external magnetic field, and  $\vec{S}$  is the vector of the electron spin operators. We use a coordinate system where the  $z$ -axis is parallel to the  $c$ -axis of the crystal ( $C_3$  symmetry axis).

In the absence of optical pumping, when the spin system is in thermal equilibrium at room temperature, all four ground states are almost equally populated. When the system is irradiated with a laser, the populations are redistributed, and the populations of the spin states  $|\pm \frac{1}{2}\rangle_g$  become large compared to those of  $|\pm \frac{3}{2}\rangle_g$ , as shown schematically in Fig. 1 [23,27]. The pumping process starts with the laser driving the transitions from the ground states to the excited states. From there, most of the population falls back to the ground states by

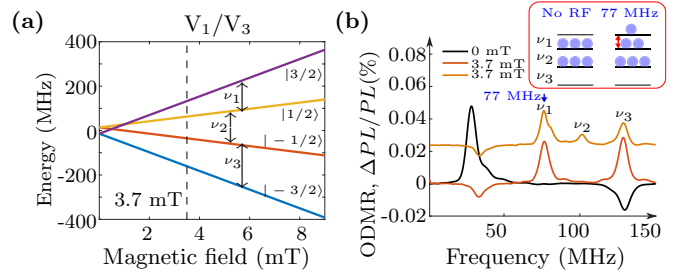


FIG. 2. (a) Energy levels of the  $V_1/V_3$  vacancy in a magnetic field  $B \parallel c$  axis. (b) ODMR signals vs frequency. The black curve is the ODMR signal measured in the absence of a magnetic field, the red curve is the ODMR signal in the 3.7 mT magnetic field, and the orange curve is the ODMR with additional 77 MHz RF in the 3.7 mT magnetic field.

spontaneous emission during the excited-state lifetime, which is  $\sim 10$  ns in the  $6H$  polytype, estimated from the linewidth of the excited-state level anticrossing (LAC) [29] and  $\sim 7.8$  ns in  $4H$  [28,30]. Although, the system can also undergo ISC to the shelving states  $|S\rangle$  [27]. The measured time constant from the excited state to  $|S\rangle$  is  $\sim 16.8$  ns for  $V_{Si}^-$  in  $4H$  [28]. From there the system returns to the ground state, with a bias for the states  $|\pm \frac{1}{2}\rangle$  over  $|\pm \frac{3}{2}\rangle$ , with a time constant 150 ns for  $V_{Si}^-$  in  $4H$  [8,17,25,28]. The exact rates from the excited state to  $|S\rangle$  and from  $|S\rangle$  to the ground state have not been measured yet for  $V_{Si}^-$  in the  $6H$ -SiC polytype, but they should be close to those in the  $4H$ -SiC polytype.

If the spins are not in thermal equilibrium and pumping stops, they relax back to the thermal equilibrium state by spin-lattice relaxation, as shown by the blue arrows in Fig. 1. Here,  $\gamma$  and  $\alpha$  are the spin-lattice relaxation rates of the  $|\pm \frac{3}{2}\rangle \leftrightarrow |\pm \frac{1}{2}\rangle$  and  $|\pm \frac{1}{2}\rangle \leftrightarrow |-\frac{1}{2}\rangle$  transitions.

### III. OPTICALLY DETECTED MAGNETIC RESONANCE

The ODMR technique is similar to the conventional electron spin resonance (ESR) technique except for the additional optical pumping and the detection part. In the ODMR technique, instead of measuring absorbed microwave or radio frequency (RF) power, an optical signal is detected, which may be PL or a transmitted or reflected laser beam [12,31–33]. The detailed description of the ODMR setup is given in Appendix B.

#### A. Continuous-wave ODMR

Figure 2(b) shows the ODMR signal measured in the absence of a magnetic field by sweeping the direct digital synthesizer (DDS) frequency as the black curve. Two peaks with different signs are observed: a positive one (i.e., increase of the PL at the application of RF) at 28 MHz and a negative one at 128 MHz. The peak at 128 MHz corresponds to the  $V_{Si}^-$  at lattice sites  $k_2$  ( $V_2$  type) and the peak at 28 MHz corresponds to  $V_{Si}^-$  at the quasicubic sites  $h$  and  $k_1$  ( $V_1/V_3$ ), which have the same zero-field splitting  $D$  [19].

Figure 2(a) shows the energy levels of  $V_1/V_3$  as a function of the magnetic field  $B$  applied  $\parallel c$  axis, calculated from the Hamiltonian given in Eq. (1). Arrows labeled with  $\nu_1$ ,  $\nu_2$ , and

$\nu_3$  represent the transition  $|+3/2\rangle \leftrightarrow |+1/2\rangle$ ,  $|+1/2\rangle \leftrightarrow |-1/2\rangle$ , and  $|-3/2\rangle \leftrightarrow |-1/2\rangle$ , respectively. With classical ODMR experiments, only two of the three allowed transitions in the spin-3/2 system are observable, since the  $\pm 1/2$  states have equal populations.

The ODMR signal recorded in a 3.7 mT magnetic field is plotted as the red curve in Fig. 2(b). The peak at 77 MHz corresponds to the  $\nu_1$  transition, and the peak at 129 MHz corresponds to the  $\nu_3$  transition. The negative peak around the 30 MHz is due the  $V_2$  type  $V_{\text{Si}}^-$ . Due to the equal populations of the  $|\pm 1/2\rangle$  levels, no peak is visible at the frequency of the  $\nu_2$  transition. To observe this transition, we added a second RF source to the setup, using it to selectively change the populations. For these experiments, the pump frequency was applied at frequency  $\nu_1$  while the second device was scanned. The output signals of both sources were combined with an RF combiner, amplified, and sent to the RF coils. The inset of Fig. 2(b) shows the modification of the populations by the pumping. Sweeping the second DDS, we recorded the ODMR signal plotted as the orange curve in Fig. 2(b) where the  $\nu_2$  transition appears at 101 MHz. The PL from the different types of vacancies cannot be separated at room temperature [20]. Therefore, the measured PL includes baseline contributions from other centers that do not depend on the magnetic resonance and results in a relatively small contrast. Further, the ODMR contrast of  $V_{\text{Si}}^-$  depends on the ratio of these spontaneous and nonradiative transitions. So, it would be interesting to find alternate laser excitation pathways that provide higher ODMR contrast as well as spin polarization.

### B. Pulsed ODMR

To measure rates and time constants, we used time-resolved ODMR. For all experiments, a laser pulse of 100 mW power and 300  $\mu\text{s}$  duration was used to initialize the  $V_{\text{Si}}^-$ , i.e., populating the states  $|\pm \frac{3}{2}\rangle$  more than the states  $|\pm \frac{1}{2}\rangle$ . After the polarization of the spin system, a sequence of RF pulses was applied to the system, as discussed in detail below. To read out the final state of the spin system, we applied a second laser pulse of duration 4  $\mu\text{s}$  and integrated the PL collected during the pulse. We averaged the signal 400 times and subtracted it from a 400 times averaged signal of a reference experiment to remove unwanted background signals. This process was repeated 20 times and again the average was taken [20].

In the following, we assume that the population  $\rho_{kk}$  of the  $\pm 3/2$  spin levels contributes a fraction  $\Delta$  more to the PL signal than the  $\pm 1/2$  spin levels [21,34]. The total PL signal  $S$ , measured with the second laser pulse, is then

$$S = S_{+\frac{3}{2}} + S_{+\frac{1}{2}} + S_{-\frac{1}{2}} + S_{-\frac{3}{2}} \quad (2)$$

with the contributions

$$\begin{aligned} S_{+\frac{3}{2}} &= (S_0 + \Delta)\rho_{11}, \\ S_{+\frac{1}{2}} &= (S_0 - \Delta)\rho_{22}, \\ S_{-\frac{1}{2}} &= (S_0 - \Delta)\rho_{33}, \\ S_{-\frac{3}{2}} &= (S_0 + \Delta)\rho_{44}, \end{aligned}$$

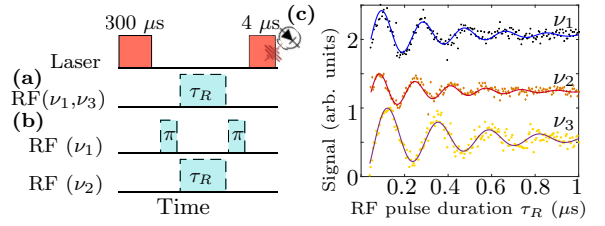


FIG. 3. Pulse sequence for measuring Rabi oscillations of (a)  $\nu_1$  and  $\nu_3$  transitions; (b)  $\nu_2$  transition. The red and blue rectangles represent the laser and RF pulses. (c) Experimental Rabi oscillations. The y-axis represents the normalized change of the PL signal, and the x-axis represents the RF pulse duration  $\tau_R$ .

from the populations of the different levels, where  $S_0$  is the average signal contribution from each level. Taking into account that the sum of the populations is  $=1$ , this can be further simplified to

$$S = 4S_0 + \Delta(\rho_{11} - \rho_{22} - \rho_{33} + \rho_{44}). \quad (3)$$

To calibrate the strength of the RF field for the pulsed excitation, we performed a measurement of Rabi oscillations for the  $\nu_1$  and  $\nu_3$  transitions of the  $V_1/V_3$  type  $V_{\text{Si}}^-$ , using the pulse sequence shown in Fig. 3(a). After the initializing laser pulse, an RF pulse of variable duration  $\tau_R$  was applied. The reference signal was obtained from an experiment without an RF pulse.

Rabi oscillations for the  $\nu_2$  transition were measured using the pulse sequence shown in Fig. 3(b). Two  $\pi$  pulses with frequency  $\nu_1$  were applied, and between them was an RF pulse with frequency  $\nu_2$  and variable duration  $\tau_R$ . The reference signal was obtained from an experiment without the RF pulses. Figure 3(c) shows the resulting experimental data for the transitions at  $\nu_1$ ,  $\nu_2$ , and  $\nu_3$ . The experimental data were fitted to the function

$$S_{\text{RF}}(\tau_R) - S_0(\tau_R) = A + B \cos(2\pi f_R \tau_R - \phi) e^{-\tau_R/T_2^R}, \quad (4)$$

where  $S_{\text{RF}}(\tau_R)$  is the signal measured with an RF pulse of duration  $\tau_R$ , and  $S_0(\tau_R)$  is the reference signal without the RF pulse. The Rabi frequencies obtained with 20 W RF power and the measured dephasing times  $T_2^R$  are given in Table I. A plot of the Rabi frequencies versus the square root of the RF power and a plot of the dephasing times versus the Rabi frequencies of the transitions are given in Appendix C.

Next, we performed free induction decay (FID) and spin-echo measurements to measure the decay of coherence of all three transitions at room temperature and in the 3.7 mT magnetic field. FID measurement include coherence decay due to homogeneous and inhomogeneous interactions. For FID measurements, we used the Ramsey scheme [35] where the

TABLE I. Parameters of the Rabi oscillations for the different transitions of  $V_1/V_3$  type  $V_{\text{Si}}^-$ .

Transition frequency	$f_R$ (MHz)	$T_2^R$ (ns)
$\nu_1$ (77 MHz)	$5.26 \pm 0.05$	$299 \pm 30$
$\nu_2$ (101 MHz)	$6.14 \pm 0.05$	$285 \pm 27$
$\nu_3$ (129 MHz)	$4.29 \pm 0.03$	$381 \pm 29$

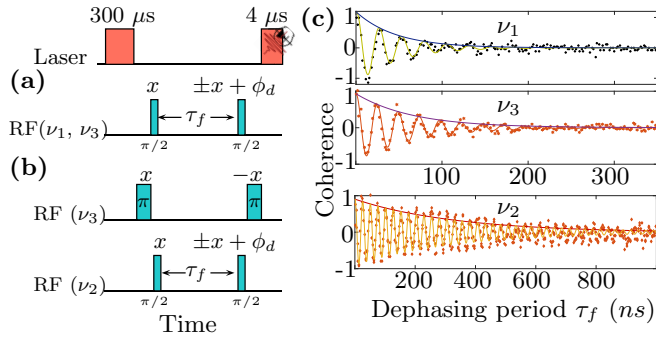


FIG. 4. Pulse sequence for measuring free induction decay of (a)  $\nu_1$  and  $\nu_3$  transitions; (b)  $\nu_2$  transition. The red and blue rectangles represent the laser and RF pulses. (c) FID signals measured at the transitions  $\nu_1$ ,  $\nu_3$ , and  $\nu_2$ . The oscillation frequency is given by the detuning frequency of the pulse sequence, which is 40 MHz in all three cases.

second  $\pi/2$  RF pulse converted the coherence into a population difference, which was then read out during the final laser pulse. Figure 4(a) shows the experimental scheme for FID measurements of transitions  $\nu_1$  and  $\nu_3$ : After the initialization by the first laser pulse, the first  $\pi/2$  RF pulse of frequency  $\nu_1$  ( $\nu_3$ ) generated the coherence, which was then allowed to precess for a time  $\tau_f$ , and then a  $\pi/2$  RF pulse with phase  $\phi_d = f_{\text{det}}\tau_f$  was applied before the readout laser pulse. We again used the difference between two experiments, where the second  $\pi/2$  RF pulses have phases  $\phi_d$  and  $\pi + \phi_d$ , respectively, to suppress unwanted background signals [20]. The pulse sequence for the measurement of the FID at  $\nu_2$  is shown in Fig. 4(b). It uses two additional  $\pi$  pulses at frequency  $\nu_3$  with a phase difference of  $\pi$ , and two  $\pi/2$  pulses at frequency  $\nu_2$ . Figure 4(c) shows the FIDs measured for  $\nu_1$ ,  $\nu_3$ , and  $\nu_2$ , respectively, with detuning of  $f_{\text{det}} = 40$  MHz, together with a fit function

$$S_{x+\phi_d} - S_{-x+\phi_d} = A \cos(2\pi f_{\text{det}}\tau_f + \phi) e^{-\tau_f/T_2^*}, \quad (5)$$

where  $S_{x+\phi_d}(\tau_f)$  and  $S_{-x+\phi_d}(\tau_f)$  are the averaged PL signals measured with the  $\pm x + \phi_d$  detection pulse. The decay time  $T_2^*$  is  $46 \pm 6$  ns for transition  $\nu_1$ ,  $333 \pm 40$  ns for transition  $\nu_2$ , and  $66 \pm 8$  ns for transition  $\nu_3$ . The longer dephasing time for the transition  $\nu_2$  ( $+1/2 \leftrightarrow -1/2$ ) is expected as it is not affected by the zero-field splitting [25,36] and therefore less affected by inhomogeneous broadening than the two transitions  $\nu_1$  and  $\nu_3$ .

To measure the coherence decay due to the homogeneous interactions, we performed the spin-echo experiment (Hahn echo) [37]. Figure 5(a) shows the pulse sequence for the spin-echo measurement of transitions  $\nu_1$  and  $\nu_3$ , and Fig. 5(b) shows the pulse sequence for transition  $\nu_2$ . The pulse sequences used to measure the spin-echo of all three transitions are similar to the corresponding FID measurement sequences except for an additional  $\pi$  pulse in the center between the two  $\pi/2$  pulses. Figure 5(c) plots the resulting data as a function of the dephasing period  $\tau_2$ , together with a fit to the function

$$S_x - S_{-x} = A e^{-(\tau_2/T_2^{\nu_i})^n}, \quad (6)$$

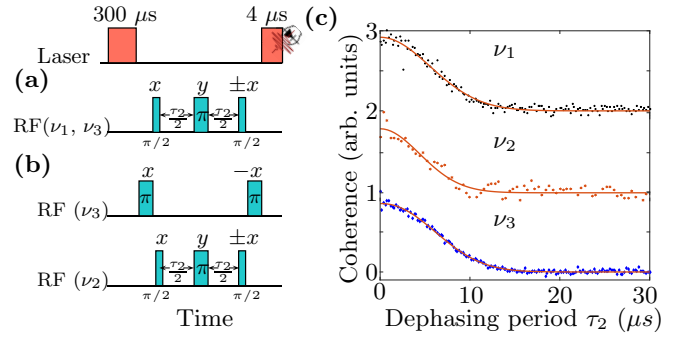


FIG. 5. Pulse sequence for spin-echo experiments at (a)  $\nu_1$  and  $\nu_3$  transitions, and (b)  $\nu_2$  transition. The red and blue rectangles represent the laser and RF pulses. (c) Spin-echo signals measured at the transitions  $\nu_1$ ,  $\nu_2$ , and  $\nu_3$ .

where  $S_x(\tau_2)$  and  $S_{-x}(\tau_2)$  are the signals measured with the  $\pm x$  pulse. The fitted parameters are  $T_2^{\nu_1} = 7.9 \pm 0.2 \mu\text{s}$ ,  $n = 2.23$  for transition  $\nu_1$ ,  $T_2^{\nu_2} = 6.2 \pm 0.3 \mu\text{s}$ ,  $n = 1.97$  for transition  $\nu_2$ , and  $T_2^{\nu_3} = 8.2 \pm 0.3 \mu\text{s}$ ,  $n = 2.17$  for transition  $\nu_3$  at room temperature and in the 3.7 mT of an external magnetic field. The ratio  $\langle T_2^{\nu_1, \nu_3} \rangle / T_2^{\nu_2} = 1.30 \pm 0.03$  agrees, within the experimental uncertainties, with the theoretical value of  $4/3$  expected for relaxation by random magnetic fields coupling to the electron spin dipole moment [38].

## IV. POPULATION RELAXATION

### A. Equation of motion

The uncontrolled interaction of a spin system with its environment has two effects on a system that has been excited from its thermal equilibrium state: it causes dephasing, i.e., loss of coherence, and a return of the system to the thermal equilibrium state [39], which is known as spin-lattice relaxation. In this process, energy is exchanged between the system and its environment (the lattice). As shown in Fig. 1, due to energy exchange between the  $V_{Si}^-$  and their environment, the populations evolve toward the equilibrium distribution with rates  $\alpha$  and  $\gamma$ , where  $\alpha$  is the rate at which the  $|\pm \frac{1}{2}\rangle_g$  spin levels equilibrate, and  $\gamma$  is the rate between the  $|\pm \frac{3}{2}\rangle_g \leftrightarrow |\pm \frac{1}{2}\rangle_g$  states. The time evolution of the four-level system can thus be described by the following equation:

$$\frac{d}{dt} \vec{\rho} = \frac{1}{2} \begin{pmatrix} -\gamma & \gamma & \alpha & \alpha \\ \gamma & -\alpha - \gamma & \alpha & \alpha \\ \alpha & \alpha & -\alpha - \gamma & \gamma \\ \alpha & \alpha & \gamma & -\gamma \end{pmatrix} \vec{\rho}, \quad (7)$$

where the population vector  $\vec{\rho}$  contains the diagonal elements  $\rho_{ii}$  of the density operator.

The eigenvalues  $\lambda_i$  and eigenvectors  $\vec{u}_i$  for Eq. (7) are

$$\vec{\lambda} = \begin{pmatrix} 0 \\ -\gamma \\ -\frac{\alpha + \gamma + \xi}{2} \\ -\frac{\alpha + \gamma - \xi}{2} \end{pmatrix}$$



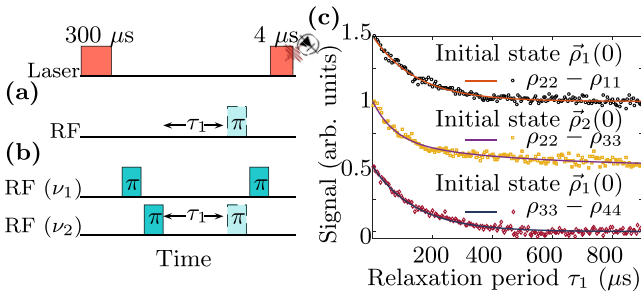


FIG. 6. Pulse sequences used to prepare specific initial states and measure the population differences (a)  $\rho_{22}(\tau_1) - \rho_{11}(\tau_1)$  and  $\rho_{33}(\tau_1) - \rho_{44}(\tau_1)$ , and (b)  $\rho_{22}(\tau_1) - \rho_{33}(\tau_1)$ . The red and blue rectangles represent the laser pulses and RF pulses. The length of the laser pulse is written above the corresponding box. (c) Resulting experimental and calculated signals [from Eq. (8)] of the population differences as a function of the delay  $\tau_1$ .

and

$$\vec{u}_i = \begin{pmatrix} 1 \\ 1 \\ 1 \end{pmatrix}, \begin{pmatrix} 1 \\ -1 \\ -1 \end{pmatrix}, \begin{pmatrix} -\gamma \\ \alpha + \xi \\ -\alpha - \xi \\ \gamma \end{pmatrix}, \begin{pmatrix} -\gamma \\ \alpha - \xi \\ -\alpha + \xi \\ \gamma \end{pmatrix},$$

respectively, where  $\xi = \sqrt{\alpha^2 + \gamma^2}$ .

The solution of Eq. (7) for an initial condition  $\vec{\rho}(0) = (a, b, c, d)^\top$  is

$$\vec{\rho}(t) = \frac{1}{4} \sum c_i e^{\lambda_i t} \vec{u}_i, \quad (8)$$

where the weights

$$\begin{aligned} c_1 &= 1, \\ c_2 &= a - b - c + d, \\ c_3 &= \frac{(a-d)(\alpha - \xi) + \gamma(b-c)}{\gamma\xi}, \\ c_4 &= -\frac{(a-d)(\alpha + \xi) + \gamma(b-c)}{\gamma\xi} \end{aligned}$$

are given by the initial conditions.

### B. Measurements

High-quality measurements of the time dependence of individual populations are difficult. We therefore measure differences  $\rho_{ii} - \rho_{kk}$  between populations. We start with two particularly simple time dependences, which can be measured with the experiments shown in Figs. 6(a) and 6(b). We first prepare an initial state with the populations  $\vec{\rho}_1(0) = (0, 0.5, 0.5, 0)^\top$ , so that  $c_1 = -c_2 = 1$  and  $c_3 = c_4 = 0$ , and the expected time dependence is

$$\vec{\rho}(t) = \frac{1}{4} (\vec{u}_1 - e^{\lambda_2 t} \vec{u}_2) = \frac{1}{4} \begin{pmatrix} 1 - e^{-\gamma t} \\ 1 + e^{-\gamma t} \\ 1 + e^{-\gamma t} \\ 1 - e^{-\gamma t} \end{pmatrix}. \quad (9)$$

The pulse sequence for the preparation of the initial state  $\vec{\rho}_1(0)$  from the unpolarized state is shown in the first row of Table II: it consists of a laser pulse of duration  $300 \mu\text{s}$ ,

TABLE II. Pulse sequences used to prepare different initial states  $\vec{\rho}_i(0)$ , where  $L$  represents a laser pulse of duration  $300 \mu\text{s}$ , and  $R^{v_i}$  are RF pulses with frequency  $\nu_i$  and flip angle  $\pi$ . Pulse sequences 1 and 2 are used in Sec. IV and 3 and 4 are used in Sec. V.

S. no.	Initial state $\vec{\rho}_i(0)$	Pulse sequence
1	$(0, 0.5, 0.5, 0)^\top$	$L$
2	$(0.5, 0.5, 0, 0)^\top$	$LR^{\nu_1}R^{\nu_2}$
3	$(0, 0.5, 0, 0.5)^\top$	$LR^{\nu_3}$
4	$(0, 0, 0.5, 0.5)^\top$	$LR^{\nu_3}R^{\nu_2}$

which is long enough to drive the system to a steady state. After the state preparation, the system is allowed to relax for a time  $\tau_1$ . To read out the final state, we apply an RF pulse with flip-angle  $\pi$  and record the PL during the measuring laser pulse. We subtract the result of this experiment from a similar experiment where the RF pulse was omitted. The resulting signal is proportional to the difference between the populations that were exchanged by the  $\pi$ -pulse. If the  $\pi$ -pulse is applied at frequency  $\nu_1$ , the signal is proportional to  $\rho_{22}(\tau_1) - \rho_{11}(\tau_1)$ , and if it is applied at  $\nu_3$ , the signal is proportional to  $\rho_{33}(\tau_1) - \rho_{44}(\tau_1)$ .

Figure 6(c) shows the resulting signals for  $\rho_{22}(\tau_1) - \rho_{11}(\tau_1)$  and  $\rho_{33}(\tau_1) - \rho_{44}(\tau_1)$  as a function of the delay  $\tau_1$ . We fit the theoretical signal of Eq. (9) to the experimental signal. From the fits, we obtain the relaxation rate  $\gamma = 6.8 \pm 0.2 \text{ ms}^{-1}$ , which corresponds to time constants  $T_1^{12} = T_1^{34} = 1/\gamma = 146.2 \pm 3.6 \mu\text{s}$  at room temperature.

To determine the second rate constant  $\alpha$ , a different initial condition is needed. We chose  $\vec{\rho}_2(0) = (0.5, 0.5, 0, 0)^\top$  and measured the population difference  $\rho_{22} - \rho_{33}$ , which we expect to depend on the relaxation delay  $\tau_1$  as

$$\rho_{22}(\tau_1) - \rho_{33}(\tau_1) = \frac{\lambda_3(\alpha - \xi)e^{\lambda_4 \tau_1} - \lambda_4(\alpha + \xi)e^{\lambda_3 \tau_1}}{2\gamma\xi}. \quad (10)$$

The pulse sequence used to prepare the initial state  $\vec{\rho}_2(0)$  from the thermal state is given in row 2 of Table II and in Fig. 6(b), which also shows the sequence for measuring the population difference  $\rho_{22} - \rho_{33}$ . For the initial state preparation, the  $300 \mu\text{s}$  laser pulse and two RF  $\pi$  pulses were applied, one with frequency  $\nu_1$  and a second with frequency  $\nu_2$ . Then the system was allowed to relax for a time  $\tau_1$  and another RF  $\pi$ -pulse with frequency  $\nu_1$  and the measuring laser pulse were applied. The result of this experiment was subtracted from a reference experiment with an additional  $\pi$ -pulse of frequency  $\nu_2$  after the delay  $\tau_1$ , as indicated in Fig. 6(b) by the dashed rectangle. Figure 6(c) shows the resulting signals for  $\rho_{22}(\tau_1) - \rho_{33}(\tau_1)$  as a function of the delay  $\tau_1$ . The theoretical signal of Eq. (10) was fitted to the experimental signals, using the value of  $\gamma$  determined before. From the fits, we obtained the relaxation rate  $\alpha = 9.3 \pm 0.4 \text{ ms}^{-1}$  and the relaxation time  $T_1^{23} = 1/\alpha = 107.3 \pm 4.9 \mu\text{s}$  at room temperature. The ratio  $\alpha/\gamma = 1.4 \pm 0.1$  agrees, within the experimental uncertainties, with the theoretical value of  $4/3$  (the ratio of the squares of the corresponding transition dipole moments) expected for relaxation by random magnetic fields coupling to the electron spin dipole moment [38].

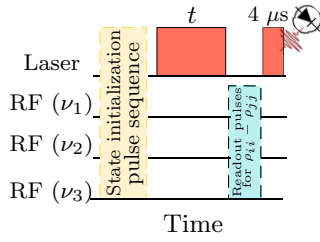


FIG. 7. Pulse sequence scheme used to prepare specific initial states and measure the evolution of the population difference  $\rho_{ii} - \rho_{jj}$  during optical pumping. Details of the initialization sequence are given in Table II, and those for the readout sequence are in Table III.

## V. OPTICAL SPIN ALIGNMENT

### A. Experiments

Initialization of quantum registers to a specific state is one of the primary requirements for the realization of any quantum device [40,41]. The  $V_{\text{Si}}^-$  spin ensemble can be initialized into the  $\pm 1/2$  spin states of the electronic ground state by laser illumination [20,23,27]. To determine the dynamics of this initialization process, we prepared the spin ensemble in different initial states, applied a laser pulse, and again measured the populations  $\vec{\rho}(t)$  as a function of the duration of the laser pulse. Figure 7 shows the pulse sequence used for preparing and measuring the population differences  $\rho_{ii} - \rho_{jj}$  during optical pumping. First, we started with the unpolarized state  $\vec{\rho}_0(0) = (1/4)(1, 1, 1, 1)^T$ . The laser pulse of duration  $t$  was applied, followed by the RF sequence given in Table III, and the PL signal was measured during the readout pulse. This PL signal was subtracted from a reference PL signal measured by a similar experiment where no RF pulse was applied. The difference signal is proportional to  $\rho_{ii} - \rho_{jj}$ . For measuring the population differences  $\rho_{22} - \rho_{11}$  and  $\rho_{33} - \rho_{44}$ , the same RF pulse sequences were used as in Sec. IV B. For measuring the population difference  $\rho_{22} - \rho_{44}$ , the RF pulse sequence given in the third row of Table III was used i.e., a  $\pi$  pulse with frequency  $\nu_2$  followed by a  $\pi$  pulse at frequency  $\nu_3$ . For measuring the population difference  $\rho_{33} - \rho_{11}$ , the RF pulse sequence is given in the fourth row of Table III: A  $\pi$  pulse at frequency  $\nu_2$  is followed by another  $\pi$  pulse at frequency  $\nu_1$ . The experimental data  $[S_{\rho_{ii}-\rho_{jj}}(t)]$  were scaled by multiplying them with a constant factor  $N$  such that the signal for  $\rho_{33} - \rho_{44}$  of the stationary state (14) prepared by a  $300 \mu\text{s}$  laser pulse matches the theoretically expected value of

TABLE III. Readout pulse sequences used to measure different population differences.  $R^i$  are RF pulses with frequency  $\nu_i$  and flip angle  $\pi$ .

S. no.	Population difference	Pulse sequence
1	$\rho_{22} - \rho_{11}$	$R^{\nu_1}$
2	$\rho_{33} - \rho_{44}$	$R^{\nu_3}$
3	$\rho_{22} - \rho_{44}$	$R^{\nu_2} R^{\nu_3}$
4	$\rho_{33} - \rho_{11}$	$R^{\nu_2} R^{\nu_1}$

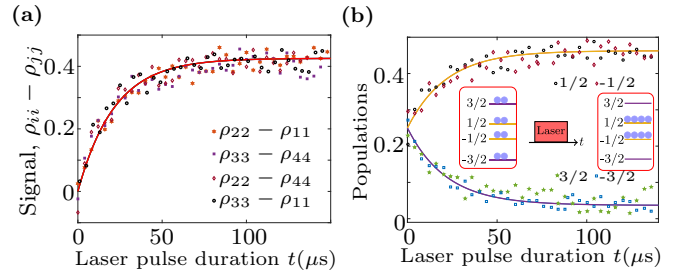


FIG. 8. (a) Population differences  $\rho_{ii} - \rho_{jj}$ , vs laser pulse duration  $t$ . Stars, squares, diamonds, and circles represent the experimentally measured signal for the population differences. The red curve represents the analytical solution, obtained by solving Eq. (15) when the system is initially unpolarized. (b) Populations as a function of the laser pulse duration  $t$ , starting from the unpolarized state.

0.37:

$$\rho_{ii} - \rho_{jj}(t) = NS_{\rho_{ii}-\rho_{jj}}(t). \quad (11)$$

While the absolute scale of the signal is not important for the goal of determining the rate constants, we use this scaling, which fixes the absolute values of the populations and allows a unique comparison between the theoretical model and the experimental data. The resulting normalized signals  $\rho_{ii} - \rho_{jj}$  are shown in Fig. 8(a).

When the  $V_{\text{Si}}^-$  is excited with a nonresonant laser, the shelving states also populate the  $m_s = \pm 3/2$  states, and the resulting spin polarization ( $P$ ) is reduced [21]. In this more general case, the population vector can be written as

$$\vec{\sigma} = \frac{1-P}{4} \hat{I} + P\vec{\rho}, \quad (12)$$

and the polarization  $P$  has been estimated as  $\approx 80\%$  [16]. Here,  $\vec{\sigma}$  represents the total ensemble's population vector, and  $\vec{\rho} = (\rho_{11}, \rho_{22}, \rho_{33}, \rho_{44})^T$  is the population vector of the spin-polarized subensemble, which can be manipulated by RF pulses. All four populations  $\rho_{11}$ ,  $\rho_{22}$ ,  $\rho_{33}$ , and  $\rho_{44}$  could be determined individually from the four experiments described above and using the normalization condition  $\rho_{11} + \rho_{22} + \rho_{33} + \rho_{44} = 1$ .

Figure 8(b) shows the evolution of the populations of the spin states during the laser pulse. Starting from the unpolarized state where all populations are  $\rho_{ii} = 1/4$ , the populations  $\rho_{22}$  and  $\rho_{33}$  grow to a limiting value of  $\approx 0.44$  while the populations  $\rho_{11}$  and  $\rho_{44}$  decrease to a limiting value of  $\approx 0.06$ .

We repeated the experiment of Fig. 7, with different initial conditions:  $\vec{\rho}_3(0) = (0, 0.5, 0, 0.5)^T$  and  $\vec{\rho}_4(0) = (0, 0, 0.5, 0.5)^T$ . The pulse sequences used for the preparation of these initial states are given in the third and fourth row of Table II, respectively. The corresponding results are shown in Figs. 9(a) and 9(b). From the measured population differences, we reconstructed the time dependence of the populations, which are shown in Figs. 9(c) and 9(d), as a function of the laser pulse duration  $t$ . The experimentally prepared initial states were  $\vec{\rho}_{3\text{exp}}(0) = (0.03, 0.47, 0.11, 0.39)^T$  and  $\vec{\rho}_{4\text{exp}}(0) = (0.06, 0.16, 0.36, 0.42)^T$ . One of the main reasons for the deviations of the experimentally prepared states from the theoretical states is the limited laser intensity, which results in incomplete polarization. This could be improved by

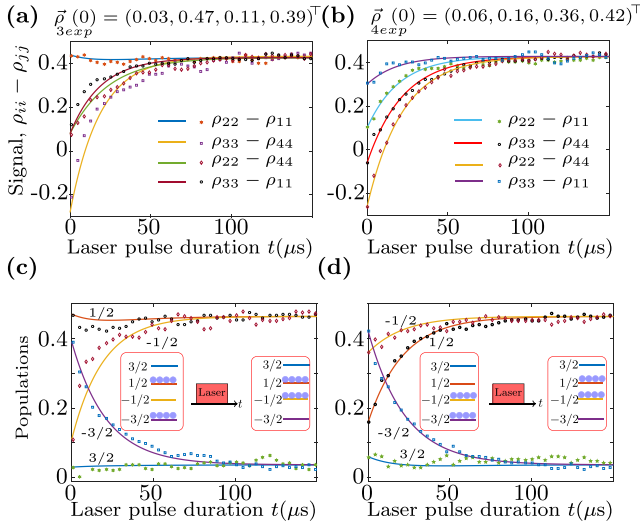


FIG. 9. (a),(b) Population differences  $\rho_{22} - \rho_{11}$ ,  $\rho_{33} - \rho_{44}$ ,  $\rho_{22} - \rho_{44}$ , and  $\rho_{33} - \rho_{11}$  as a function of the laser pulse duration  $t$ . The experimental data are represented as points, and the corresponding analytical solutions Eq. (15) are represented as curves. In (a), the initial condition was  $\vec{\rho}_{3\text{exp}}(0) = (0.03, 0.47, 0.11, 0.39)^\top$  and in (b)  $\vec{\rho}_{4\text{exp}}(0) = (0.06, 0.16, 0.36, 0.42)^\top$ . (c),(d) Populations as a function of the laser pulse duration  $t$  for the initial state (c)  $\vec{\rho}_{3\text{exp}}$  and (d)  $\vec{\rho}_{4\text{exp}}$ .

using a tighter focus of the laser beam. Other causes are imperfections in the RF pulses and relaxation.

### B. Model and rate constants

The laser pulse transfers population from the spin levels  $|\pm \frac{3}{2}\rangle$  through the shelving state to  $|\pm \frac{1}{2}\rangle$ , as indicated in Fig. 8(b). Figures 8 and 9 show that during the laser pulse, the populations of the  $|\pm \frac{1}{2}\rangle$  states increase to values close to 0.5, while the populations of the  $|\pm \frac{3}{2}\rangle$  states are strongly depleted.

Based on these experimental results, and assuming that the lifetimes in the excited state and the shelving states are short compared to the pumping time, we use the following equations for modeling the dynamics of the system:

$$\begin{aligned} \frac{d}{dt} \vec{\rho} &= \frac{1}{2} \begin{pmatrix} -\gamma - 2\delta & \gamma & & \\ \gamma + \delta & -\alpha - \gamma - \delta & \alpha + \delta & \delta \\ \delta & \alpha + \delta & -\alpha - \gamma - \delta & \gamma + \delta \\ & & \gamma & -\gamma - 2\delta \end{pmatrix} \vec{\rho}, \end{aligned} \quad (13)$$

where  $\delta$  is the rate at which population is pumped from the states  $|\pm \frac{3}{2}\rangle$  to  $|\pm \frac{1}{2}\rangle$ . The resulting stationary state is

$$\vec{\rho}_{\text{st}} = \frac{\gamma}{4(\gamma + \delta)} \begin{pmatrix} 1 \\ 1 \\ 1 \\ 1 \end{pmatrix} + \frac{\delta}{2(\gamma + \delta)} \begin{pmatrix} 0 \\ 1 \\ 1 \\ 0 \end{pmatrix}, \quad (14)$$

which approaches  $(0, \frac{1}{2}, \frac{1}{2}, 0)^\top$  for  $\delta \gg \gamma$ .

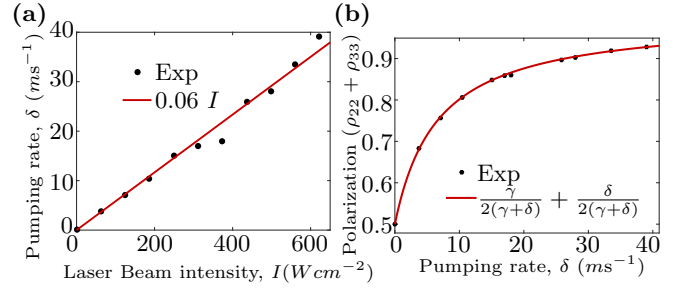


FIG. 10. Plot of (a) pumping rates with the laser beam intensity, (b) polarization with pumping rate.

The eigenvalues and eigenvectors for Eq. (13) are

$$\begin{aligned} \vec{\lambda}^{\text{op}} &= \begin{pmatrix} 0 \\ -\gamma - \delta \\ -\frac{\alpha + \gamma + \xi}{2} - \delta \\ -\frac{\alpha + \gamma - \xi}{2} - \delta \end{pmatrix}, \\ \vec{v}_i &= \left\{ \begin{pmatrix} 1 \\ \frac{\gamma + 2\delta}{\gamma} \\ \frac{\gamma + 2\delta}{\gamma} \\ 1 \end{pmatrix}, \begin{pmatrix} 1 \\ -1 \\ -1 \\ 1 \end{pmatrix}, \begin{pmatrix} -1 \\ \frac{\alpha^2 + \xi(\delta + \alpha) + \delta(\alpha - \gamma)}{\alpha\gamma + \delta(\alpha + \gamma - \xi)} \\ -\frac{\alpha + \xi}{\gamma} \\ 1 \end{pmatrix}, \right. \\ &\quad \left. \begin{pmatrix} -1 \\ \frac{\alpha^2 - \xi(\delta + \alpha) + \delta(\alpha - \gamma)}{\alpha\gamma + \delta(\alpha + \gamma + \xi)} \\ -\frac{\alpha + \xi}{\gamma} \\ 1 \end{pmatrix} \right\}, \end{aligned}$$

respectively. The solution of Eq. (13) for an initial state  $\vec{\rho}(0) = (a, b, c, d)^\top$  is

$$\vec{\rho}(t) = \frac{1}{4} \sum p_i e^{\lambda_i^{\text{op}} t} \vec{v}_i, \quad (15)$$

where

$$\begin{aligned} p_1 &= \frac{\gamma}{\gamma + \delta}, \\ p_2 &= \frac{\gamma(a - b - c + d) + 2\delta(a + d)}{\gamma + \delta}, \\ p_3 &= \frac{\gamma(b - c) - (\xi - \alpha)(a - d)}{\xi}, \\ p_4 &= \frac{\gamma(c - b) - (\xi + \alpha)(a - d)}{\xi}. \end{aligned}$$

The resulting expressions for the case in which the initial state is the depolarized state is given in Appendix D. The calculated population differences are plotted in Figs. 8(a), 9(a), and 9(b), and the populations are plotted in Figs. 8(b), 9(c), and 9(d). The best fits with the experimental data, which were measured with a laser intensity  $I = 622.64 \text{ W/cm}^2$ , were obtained for the rate constant  $\delta = 39 \pm 3 \text{ ms}^{-1}$ . For  $\alpha$  and  $\gamma$ , we used the values determined in Sec. IV.

Taking additional data with different laser intensities, we found that the pumping rate  $\delta$  increases linearly with the intensity, i.e.,  $\delta (\text{ms}^{-1}) = 0.06 \pm 0.01 I (\text{W cm}^{-2})$ , as shown in Fig. 10(a). This indicates that the rate is limited by the

population of the shelving state, which is far from being saturated under our experimental conditions. Figure 10(b) shows the spin polarization, measured as the sum of the  $\pm 1/2$  states after a laser pulse of  $300 \mu\text{s}$  as a function of the pumping rate  $\delta$ .

## VI. DISCUSSION AND CONCLUSION

Silicon vacancy centers in SiC have shown promising results for quantum sensing, single-photon emitters, and applications as light-matter interfaces and other quantum technologies. In this work, we have demonstrated the coherent control of all four levels of the  $V_1/V_3$ -type  $V_{\text{Si}}^-$ . We measured the Rabi frequency of all three RF transitions and the corresponding relaxation rates  $\alpha$  (for  $|+1/2\rangle \leftrightarrow |-1/2\rangle$ ) and  $\gamma$  (for  $|\pm 3/2\rangle \leftrightarrow |\pm 1/2\rangle$ ) by fitting the data with the proposed relaxation model. In general, the relaxation of a spin-3/2 system can be described by three relaxation modes with three time constants, which have been termed the spin dipole ( $T_p$ ), quadrupole ( $T_d$ ), and octupole ( $T_f$ ) [25,42–44]. For a dipolelike perturbation, the spin-relaxation times are  $T_p/3 = T_d = 2T_f$ ,  $\alpha = (2/3)T_d^{-1}$ , and  $\gamma = (1/2)T_d^{-1}$  as discussed theoretically in the case of a fluctuating magnetic field acting on a  $V_{\text{Si}}^-$  in SiC [25,38]. The ratio of the experimentally measured values of  $\alpha$  and  $\gamma$  is close to this theoretical value. It has recently been demonstrated that for  $V_2$ -type  $V_{\text{Si}}^-$  in 4H-SiC, this is not the case due to mixing the octupole and dipole relaxation modes since a perturbation with dipole symmetry cannot mix different order poles [43].

We also determined the dynamics of the optical initialization process by preparing the system in three different initial states and measuring the population dynamics during a laser pulse. The laser illumination transfers the population from  $\pm 3/2$  to  $\pm 1/2$  spin states for all three initial states. To interpret the resulting data, we proposed a simple rate equation model for this process, and we were able to determine all relevant rate constants from the experimental data. According to Fig. 10(b), the spin polarization of subensemble  $\rho$  approaches unity at intensities  $>200 \text{ W/cm}^2$ . As mentioned above, with the nonresonant laser excitation, the shelving states also populate the  $\pm 3/2$  states, resulting in reduced spin polarization of the total ensemble  $\sigma$ , which can be improved by using resonant optical excitation [21]. In conclusion, we are confident that our results will contribute to a better understanding of this fascinating system and pave the way to more useful applications.

## ACKNOWLEDGMENTS

This work was supported by the Deutsche Forschungsgemeinschaft in the frame of the ICRC TRR 160 (Project No. C7) and by RFBR, Project no. 19-52-12058. SIMS measurements were performed using the Center of Multi-User Equipment “Material Science and Diagnostics for Advanced Technologies” (Ioffe Institute, Russia) facility supported by the Russian Ministry of Science (The Agreement ID RFMEFI62119X0021).

## APPENDIX A: SAMPLE PREPARATION

The experiments were carried out on the same sample as used in our previous work [20]. This sample was iso-

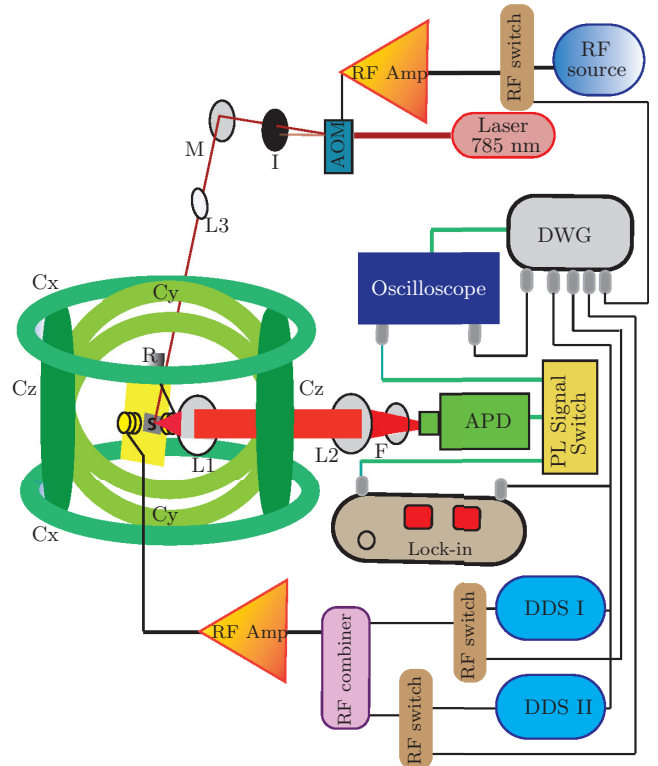


FIG. 11. Experimental setup for measuring ODMR. The red line from the laser represents the laser beam. The acousto-optic modulator (AOM) generates the laser pulses. Ellipsoids labeled  $M$ ,  $L$ , and  $F$  represent mirrors, convex lenses, and a long-pass filter, respectively. The RF is applied using a three-turn Helmholtz coil-pair made of  $100 \mu\text{m}$  diameter copper wire placed perpendicular to the  $c$ -axis, in series with a  $50 \Omega$  resistor which is represented by a rectangle labeled  $R$ . The gray rectangle labeled  $S$  is the SiC sample, which is placed between the RF coils. The three orthogonal ring-pairs  $C_x$ ,  $C_y$ , and  $C_z$  represent Helmholtz coils for generating a static magnetic field in an arbitrary direction. Rounded rectangles labeled DWG, APD, and DDS represent a digital word generator, an avalanche photodetector module, and direct digital synthesizers, respectively.

topically enriched in  $^{28}\text{Si}$  and  $^{13}\text{C}$ . As the source of a  $^{28}\text{Si}$  isotope, ready-made silicon available in the form of small pieces (1–3 mm) with an isotope composition of 99.999%  $^{28}\text{Si}$  was used. Carbon powder enriched to 15% in  $^{13}\text{C}$  was used as the  $^{13}\text{C}$  source. The SiC crystal was grown at a growth rate of  $\approx 100 \mu\text{m/h}$  on a (0001) Si face at a temperature of  $2300^\circ\text{--}2400^\circ\text{C}$  in an argon atmosphere. Following the growth of the SiC crystal, the wafer was machined and cut. Secondary ion mass spectroscopy (SIMS) was used to evaluate the isotope composition.  $^{28}\text{Si}$ ,  $^{29}\text{Si}$ , and  $^{30}\text{Si}$  have concentrations of 99.918%, 0.076%, and 0.006%, respectively.  $^{12}\text{C}$  and  $^{13}\text{C}$  have concentrations of 95.278% and 4.722%, respectively. At room temperature, the crystal was irradiated with electrons of an energy 2 MeV and with a dose of  $10^{18} \text{ cm}^{-2}$  to create  $V_{\text{Si}}^-$  centers.

## APPENDIX B: ODMR SETUP

Figure 11 shows the setup used for the cw- and time-resolved ODMR measurements. Our light source was a



785 nm laser diode (Thorlabs LD785-SE400) with a maximum power of 400 mW, which was driven by a Thorlabs laser diode controller (LDC202C series) with a thermoelectric temperature controller (TED 200C). For generating the laser pulses, we used an acousto-optical modulator (AOM; NEC model OD8813A). The RF pulses were generated by an RF switch (Mini-Circuits ZASWA-2-50DR+, dc-5 GHz). The TTL (transistor transistor logic) pulses that control the timing were generated by a digital word generator (DWG; SpinCore PulseBlaster ESR-PRO PCI card).

We used three orthogonal Helmholtz coil-pairs for applying the static magnetic field in an arbitrary direction. A highly stable linear current source (Servowatt, three-channel DCP-390/30) delivers currents up to 15A to the coils. The currents were controlled individually by an analog control voltage.

The RF signal was generated with a direct digital synthesizer (DDS) AD9915 from Analog Devices, which generates signals up to 1 GHz. The RF pulses that drive the spins were generated by an RF switch, amplified with a Mini-Circuits LZY-1, 50 W amplifier, and applied to the SiC sample through a handmade Helmholtz-pair of RF coils with a diameter of 2.5 mm and three turns in each coil from 100  $\mu\text{m}$  diameter wire terminated with a 50  $\Omega$  resistor. A laser beam was focused on the sample using a convex lens (L3 in Fig. 11) of focal length 20 cm. The PL from the sample was collected with a pair of lenses (L1 and L2 with focal lengths 5 and 15 cm, respectively), sent through a 850-nm-long pass filter to suppress scattered laser light and to an avalanche photodiode (APD) module with a frequency range from dc to 10 MHz (C12703 series from Hamamatsu). The signal from the APD was recorded with a USB card (PicoScope 2000 series) attached to a computer (for pulsed measurements) or to a lock-in amplifier (SRS model SR830 DSP) for cw-ODMR.

To measure the cw-ODMR signal, we used the setup shown in Fig. 11, with the RF switched on for continuous laser irradiation and the APD connected to the lock-in amplifier. The DWG was used to modulate the amplitude of the RF field, and the APD signal was demodulated with the lock-in amplifier whose reference signal was supplied by the DWG.

For the time-resolved ODMR, the APD shown in Fig. 11 was connected to the PicoScope USB card. The RF pulses were generated using DDSs and RF switches and applied between the state initialization and measurement.

### APPENDIX C: POWER DEPENDENCE OF RABI OSCILLATIONS

#### Rabi with RF power

Figure 12(a) shows the measured Rabi frequencies of the  $\nu_1$ ,  $\nu_2$ , and  $\nu_3$  transitions measured versus the square root of the applied RF power. The experimental data were fitted to the function

$$f_R(\sqrt{\text{RF power}}) = r_i \sqrt{\text{RF power}}. \quad (\text{C1})$$

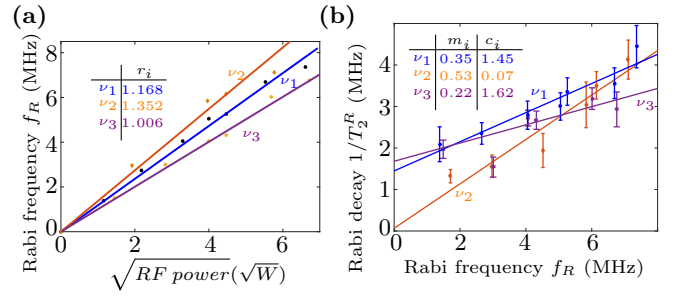


FIG. 12. (a) Plot of the experimentally measured Rabi frequency vs the square root of RF power. (b) Plot of the Rabi decay time  $T_2^R$  of different transitions vs the Rabi frequency.

The fit parameters  $r_i$  are given in the second column of Table IV for the  $\nu_1$ ,  $\nu_2$ , and  $\nu_3$  transitions. The ratio of the three Rabi frequencies is  $1.173 \pm 0.164 : 2 : 1.149 \pm 0.132$ , which is close to the theoretically expected value of  $\sqrt{3} : 2 : \sqrt{3}$ , i.e., the ratio of the transition dipole matrix elements of a spin 3/2 [43,45]. The deviation appears to be related to reflections in the circuit that feeds RF power to the sample, which generates standing waves and increases with the RF frequency. In Fig. 12(a), we measured the forward RF power instead of actual RF current in the coil, which is not easily accessible. Figure 12(b) shows the plot of the Rabi decay times of the  $\nu_1$ ,  $\nu_2$  and  $\nu_3$  transitions at different Rabi frequencies. The experimental data were fitted to the function

$$\frac{1}{T_2^R}(f_R) = m_i f_R + c_i. \quad (\text{C2})$$

The fitted parameters  $m_i$  and  $c_i$  are given in the third and fourth columns of Table IV for the  $\nu_1$ ,  $\nu_2$ , and  $\nu_3$  transitions. The differences between the  $T_2^R$  of  $\nu_1$  and  $\nu_3$  transitions are within the error margins and appear not significant. At the lower Rabi frequency, the longer dephasing time  $T_2^R$  for the transition  $\nu_2$  is expected as it is less affected by inhomogeneous broadening than the two transitions  $\nu_1$  and  $\nu_3$  [25,36].

### APPENDIX D: TIME DEPENDENCES FOR SPECIFIC INITIAL CONDITIONS

This Appendix provides two specific solutions for the population dynamics without and with the laser field, for two different initial conditions. For the initial state  $\bar{\rho}_2(0) = \frac{1}{2}(1, 1, 0, 0)^T$ , the solution of the relaxation dynamics Eq. (8)

TABLE IV. Fitting parameters of Eqs. (C1) and (C2) for the different transitions of the  $V_1/V_3$  type  $V_{\text{Si}^-}$ .

Transitions	$r_i$	$m_i$	$c_i$
$\nu_1$	$1.168 \pm 0.062$	$0.35 \pm 0.13$	$1.45 \pm 0.66$
$\nu_2$	$1.352 \pm 0.106$	$0.53 \pm 0.24$	$0.07 \pm 1.24$
$\nu_3$	$1.006 \pm 0.041$	$0.22 \pm 0.16$	$1.62 \pm 0.84$

is

$$\begin{aligned}\rho_{11}(t) &= \frac{\lambda_3 e^{\lambda_4 t} + \lambda_4 e^{\lambda_3 t} + \xi}{4\xi}, \\ \rho_{22}(t) &= \frac{\lambda_3(\alpha - \xi)e^{\lambda_4 t} - \lambda_4(\alpha + \xi)e^{\lambda_3 t} + \gamma\xi}{4\gamma\xi}, \\ \rho_{33}(t) &= \frac{\lambda_3(-\alpha + \xi)e^{\lambda_4 t} + \lambda_4(\alpha + \xi)e^{\lambda_3 t} + \gamma\xi}{4\gamma\xi}, \\ \rho_{44}(t) &= \frac{-\lambda_3 e^{\lambda_4 t} + \lambda_4 e^{\lambda_3 t} + \xi}{4\xi}.\end{aligned}$$

For the initial state  $\bar{\rho}_0(0) = \frac{1}{4}(1, 1, 1, 1)^\top$ , the solution of the optical pumping dynamics Eq. (15) is

$$\rho_{11} = \rho_{44} = -\frac{\gamma + \delta e^{\lambda_2^{\text{op}} t}}{4\lambda_2^{\text{op}}}, \quad (\text{D1})$$

$$\rho_{22} = \rho_{33} = -\frac{\gamma + 2\delta - \delta e^{\lambda_2^{\text{op}} t}}{4\lambda_2^{\text{op}}}. \quad (\text{D2})$$

- 
- [1] A. L. Falk, B. B. Buckley, G. Calusine, W. F. Koehl, V. V. Dobrovitski, A. Politi, C. A. Zorman, P. X.-L. Feng, and D. D. Awschalom, *Nat. Commun.* **4**, 1819 (2013).
- [2] M. Widmann, S.-Y. Lee, T. Rendler, N. T. Son, H. Fedder, S. Paik, L.-P. Yang, N. Zhao, S. Yang, I. Booker *et al.*, *Nat. Mater.* **14**, 164 (2015).
- [3] D. J. Christle, A. L. Falk, P. Andrich, P. V. Klimov, J. U. Hassan, N. T. Son, E. Janzén, T. Ohshima, and D. D. Awschalom, *Nat. Mater.* **14**, 160 (2015).
- [4] P. Baranov, V. A. Soltamov, A. A. Soltamova, G. V. Astakhov, and V. D. Dyakonov, in *Silicon Carbide and Related Materials 2012*, Materials Science Forum Vol. 740 (Trans Tech, Bäch, Switzerland, 2013), pp. 425–430.
- [5] A. N. Anisimov, V. A. Soltamov, I. D. Breev, R. A. Babunts, E. N. Mokhov, G. V. Astakhov, V. Dyakonov, D. R. Yakovlev, D. Suter, and P. G. Baranov, *AIP Adv.* **8**, 085304 (2018).
- [6] A. Anisimov, D. Simin, V. A. Soltamov, S. P. Lebedev, P. G. Baranov, G. V. Astakhov, and V. Dyakonov, *Sci. Rep.* **6**, 33301 (2016).
- [7] W. F. Koehl, B. B. Buckley, F. J. Heremans, G. Calusine, and D. D. Awschalom, *Nature (London)* **479**, 84 (2011).
- [8] D. Riedel, F. Fuchs, H. Kraus, S. Vāth, A. Sperlich, V. Dyakonov, A. A. Soltamova, P. G. Baranov, V. A. Ilyin, and G. V. Astakhov, *Phys. Rev. Lett.* **109**, 226402 (2012).
- [9] O. O. Soykal, P. Dev, and S. E. Economou, *Phys. Rev. B* **93**, 081207(R) (2016).
- [10] M. W. Doherty, N. B. Manson, P. Delaney, F. Jelezko, J. Wrachtrup, and L. C. Hollenberg, *Phys. Rep.* **528**, 1 (2013).
- [11] D. Suter and F. Jelezko, *Prog. Nucl. Magn. Reson. Spectrosc.* **98**, 50 (2017).
- [12] D. Suter, *Magn. Res.* **1**, 115 (2020).
- [13] A. L. Falk, P. V. Klimov, V. Ivády, K. Szász, D. J. Christle, W. F. Koehl, A. Gali, and D. D. Awschalom, *Phys. Rev. Lett.* **114**, 247603 (2015).
- [14] F.-F. Yan, J.-F. Wang, Q. Li, Z.-D. Cheng, J.-M. Cui, W.-Z. Liu, J.-S. Xu, C.-F. Li, and G.-C. Guo, *Phys. Rev. Appl.* **10**, 044042 (2018).
- [15] A. L. Falk, P. V. Klimov, B. B. Buckley, V. Ivády, I. A. Abrikosov, G. Calusine, W. F. Koehl, A. Gali, and D. D. Awschalom, *Phys. Rev. Lett.* **112**, 187601 (2014).
- [16] V. A. Soltamov, A. A. Soltamova, P. G. Baranov, and I. I. Proskuryakov, *Phys. Rev. Lett.* **108**, 226402 (2012).
- [17] T. Biktajirov, W. G. Schmidt, U. Gerstmann, B. Yavkin, S. Orlinskii, P. Baranov, V. Dyakonov, and V. Soltamov, *Phys. Rev. B* **98**, 195204 (2018).
- [18] E. Sörman, N. T. Son, W. M. Chen, O. Kordina, C. Hallin, and E. Janzén, *Phys. Rev. B* **61**, 2613 (2000).
- [19] J. Davidsson, V. Ivády, R. Armiento, T. Ohshima, N. T. Son, A. Gali, and I. A. Abrikosov, *Appl. Phys. Lett.* **114**, 112107 (2019).
- [20] H. Singh, A. N. Anisimov, S. S. Nagalyuk, E. N. Mokhov, P. G. Baranov, and D. Suter, *Phys. Rev. B* **101**, 134110 (2020).
- [21] R. Nagy, M. Niethammer, M. Widmann, Y.-C. Chen, P. Udvarhelyi, C. Bonato, J. U. Hassan, R. Karhu, I. G. Ivanov, N. T. Son *et al.*, *Nat. Commun.* **10**, 1954 (2019).
- [22] D. Simin, H. Kraus, A. Sperlich, T. Ohshima, G. V. Astakhov, and V. Dyakonov, *Phys. Rev. B* **95**, 161201(R) (2017).
- [23] H. Kraus, V. Soltamov, D. Riedel, S. Vāth, F. Fuchs, A. Sperlich, P. Baranov, V. Dyakonov, and G. Astakhov, *Nat. Phys.* **10**, 157 (2014).
- [24] M. E. Bathen, A. Galeckas, J. Müting, H. M. Ayedh, U. Grossner, J. Coutinho, Y. K. Frodason, and L. Vines, *npj Quantum Inf.* **5**, 111 (2019).
- [25] V. Soltamov, C. Kasper, A. Poshakinskiy, A. Anisimov, E. Mokhov, A. Sperlich, S. Tarasenko, P. Baranov, G. Astakhov, and V. Dyakonov, *Nat. Commun.* **10**, 1678 (2019).
- [26] L.-P. Yang, C. Burk, M. Widmann, S.-Y. Lee, J. Wrachtrup, and N. Zhao, *Phys. Rev. B* **90**, 241203(R) (2014).
- [27] P. G. Baranov, A. P. Bundakova, A. A. Soltamova, S. B. Orlinskii, I. V. Borovykh, R. Zondervan, R. Verberk, and J. Schmidt, *Phys. Rev. B* **83**, 125203 (2011).
- [28] F. Fuchs, B. Stender, M. Trupke, D. Simin, J. Pflaum, V. Dyakonov, and G. Astakhov, *Nat. Commun.* **6**, 7578 (2015).
- [29] G. Astakhov, D. Simin, V. Dyakonov, B. Yavkin, S. Orlinskii, I. Proskuryakov, A. Anisimov, V. Soltamov, and P. Baranov, *Appl. Magn. Reson.* **47**, 793 (2016).
- [30] T. C. Hain, F. Fuchs, V. A. Soltamov, P. G. Baranov, G. V. Astakhov, T. Hertel, and V. Dyakonov, *J. Appl. Phys.* **115**, 133508 (2014).
- [31] W. M. Chen, Optically detected magnetic resonance of defects in semiconductors, in *EPR of Free Radicals in Solids: Trends in Methods and Applications*, edited by A. Lund and M. Shiotani (Springer, Boston, 2003), pp. 601–625.
- [32] S. Depinna and B. Cavenett, *J. Phys. C* **15**, L489 (1982).
- [33] L. Langof, E. Ehrenfreund, E. Lifshitz, O. I. Micic, and A. J. Nozik, *J. Phys. Chem. B* **106**, 1606 (2002).
- [34] S. G. Carter, O. O. Soykal, P. Dev, S. E. Economou, and E. R. Glaser, *Phys. Rev. B* **92**, 161202(R) (2015).
- [35] N. F. Ramsey, *Phys. Rev.* **78**, 695 (1950).
- [36] M. Eickhoff and D. Suter, *J. Magn. Reson.* **166**, 69 (2004).
- [37] E. L. Hahn, *Phys. Rev.* **80**, 580 (1950).

- [38] N. Bloembergen, E. M. Purcell, and R. V. Pound, *Phys. Rev.* **73**, 679 (1948).
- [39] A. Abragam, *The Principles of Nuclear Magnetism* (Oxford University Press, Oxford, UK, 1961).
- [40] D. P. DiVincenzo, *Fortschr. Phys.: Prog. Phys.* **48**, 771 (2000).
- [41] J. Stolze and D. Suter, *Quantum Computing: A Short Course from Theory to Experiment*, 2nd ed. (Wiley-VCH, Berlin, 2008).
- [42] S. A. Tarasenko, A. V. Poshakinskiy, D. Simin, V. A. Soltamov, E. N. Mokhov, P. G. Baranov, V. Dyakonov, and G. V. Astakhov, *Phys. Status Solidi B* **255**, 1870101 (2018).
- [43] A. J. Ramsay and A. Rossi, *Phys. Rev. B* **101**, 165307 (2020).
- [44] J. R. van der Maarel, *Conc. Magn. Reson. Pt. A* **19A**, 97 (2003).
- [45] N. Mizuochi, S. Yamasaki, H. Takizawa, N. Morishita, T. Ohshima, H. Itoh, and J. Isoya, *Phys. Rev. B* **66**, 235202 (2002).